MICROWAVE ASSISTED SYNTHESIS OF RARE EARTH IONS DOPED LANTHANUM ORTHOBORATE, THEIR CHARACTERIZATIONS AND INVESTIGATIONS OF LUMINESCENCE PROPERTIES

A THESIS SUBMITTED TO

THE GRADUATE SCHOOL OF NATURAL AND APPLIED SCIENCES

OF

MIDDLE EAST TECHNICAL UNIVERSITY

BY

CANSIN BADAN

IN PARTIAL FULFILLMENT OF THE REQUIREMENTS

FOR

THE DEGREE OF MASTER OF SCIENCE

IN

CHEMISTRY

JUNE, 2012

Approval of the thesis:

MICROWAVE ASSISTED SYNTHESIS OF RARE EARTH ORTHOBORATES AND THEIR STRUCTURAL ANALYSIS

submitted by **CANSIN BADAN** in partial fulfillment of the requirements for the degree of **Master of Science in Chemistry Department, Middle East Technical University** by,

Prof. Dr. Canan Özgen _____
Dean, Graduate School of **Natural and Applied Sciences**

Prof. Dr. İlker Özkan _____
Head of Department, **Chemistry**

Assoc. Prof. Dr. Ayşen Yılmaz _____
Supervisor, **Chemistry Dept., METU**

Assoc. Prof. Dr. Okan Esentürk _____
Co-Supervisor, **Chemistry Dept., METU**

Examining Committee Members

Prof. Dr. Ceyhan Kayran _____
Chemistry Dep., METU

Assoc. Prof. Dr. Ayşen Yılmaz _____
Chemistry Dept., METU

Assoc. Prof. Dr. Okan Esentürk _____
Chemistry Dept., METU

Assoc. Prof. Dr. Mehmet Fatih Danışman _____
Chemistry Dep., METU

Prof. Dr. Nurşen Altuntaş Öztaş _____
Chemistry Dep., Hacettepe Uni.

DATE: _____

I hereby declare that all information in this document has been obtained and presented in accordance with academic rules and ethical conduct. I also declare that, as required by these rules and conduct, I have fully cited and referenced all material and results that are not original to this work.

Name & Last Name: Cansın Badan

Signiture:

ABSTRACT

MICROWAVE ASSISTED SYNTHESIS OF RARE EARTH IONS DOPED LANTHANUM ORTHOBORATE, THEIR CHARACTERIZATIONS AND INVESTIGATIONS OF LUMINESCENCE PROPERTIES

Badan, Cansın

M. Sc., Department of Chemistry

Supervisor: Assoc. Prof. Dr. Ayşen Yılmaz

Co-Supervisor: Assoc. Prof. Dr. Okan Esentürk

June 2012, 58 pages

Lanthanum orthoborate ($LaBO_3$) has aroused interest of scientists for many decades because of their remarkable properties and potential applications. They provide favorable magnetic properties for various applications. Additionally, they possess high VUV transparency and exceptional optical damage when they compose with rare earth elements.

This study comprises the synthesis of pure lanthanum orthoborate, europium, dysprosium and terbium doped lanthanum orthoborate by two methods with

three fuels, citric acid, glycine and urea. $LaBO_3$ has already been synthesized by various methods, however; in this work, two alternative roads are suggested, microwave assisted method and sol-gel microwave assisted method. The second task of the work is to find out the best luminescent product by altering the synthesis conditions, type of the doping material and the doping amount of the rare earth element.

For the microwave assisted combustion method, urea was used as a fuel. After synthesis in the microwave oven, further heating up to 950° C was performed. For the microwave assisted sol-gel method, citric acid and glycine were used. After obtaining the gel mixture, the product is synthesized in the microwave oven at 1200 W for ten minutes. For this route, again 950° C heating for 2 hours was performed.

Powder X-ray diffraction method was employed for the characterization of the material. The morphological properties of doped and un-doped materials were studied by SEM (Scanning Electron Microscope) and TEM (Transmission Electron Microscope). Besides, FT-IR (Fourier Transform Infra red) spectrometry analyses were performed to detect the differences in the bond structure and also to identify the corresponding bands. Luminescence studies were performed to detect the best emission intensities by using Fluorescence spectroscopy.

The XRD patterns confirmed that lanthanum orthoborate production was successful by three precursors. The space group is *Pnma,* and the crystal system is orthorhombic with the unit cell dimensions; a= 5.8761(1) Å, b= 5.10535(9) Å c= 8.252(1) Å. SEM images showed that lanthanum orthoborate powders tend to agglomerate and have a disordered morphology. Products synthesized by

three precursors gave different particle sizes and it is observed that the dopant has an effect on the size. FT-IR studies show the typical $LABO_3$ bands which also corroborate the successful production. Luminescence studies showed that urea precursor gives rise to the most intensive emission intensities.

Keywords: Lanthanum orthoborate, europium, dysprosium, terbium, luminescence, citric acid, urea, glycine, microwave assisted, sol-gel

ÖZ

NADİR TOPRAK ELEMENTİ İYONLARI KATKILANMIŞ LANTAN ORTOBORAT BİLEŞİKLERİNİN MİKRODALGA YARDIMIYLA SENTEZLENMESİ, KARAKTERİZASYONU VE LUMİNESAN ÖZELLİKLERİNİN İNCELENMESİ

Badan, Cansın
Yüksek Lisans, Kimya Bölümü
Tez Yöneticisi: Doç. Dr. Ayşen Yılmaz
Ortak Tez Yöneticisi: Doç. Dr. Okan Esentürk

Haziran 2012, 58 sayfa

Lantan ortoborat (LaBO3) geniş potansiyel uygulama alanları ve kayda değer özelliklerinden ötürü son yıllarda araştırmacıların dikkati çekmektedir. Bu malzemeler, birçok uygulama alanları için etkileyici magnetik özelliklere sahiptir. Bunun yanında, yüksek Vakum Ultra Viyole (VUV) şeffaflığı ve nadir toprak elementleriyle birleştiklerinde ortaya çıkan sıra dışı optik hasar eşiği bu malzemelerin özelliklerindendir.

Bu çalışmanın birinci kısmı, saf lantan ortoborat'ın; evropiyum, disprosyum ve terbiyum katkılı lantan ortoborat'ın mikrodalga destekli sentezi ve mikrodalga

destekli sol-jel metoduyla üç ayrı yakıt (sitrik asit, glisin ve üre) kullanarak sentezlenmesini ve katkılanmasını içermektedir. Lantan ortoborat günümüzde farklı yöntemlerle sentezlenmektedir, ancak, bu çalışmada iki alternatif yol önerilmektedir. Çalışmanın ikinci kısmı, sentez yöntemindeki değişiklikler, nadir toprak elementinin cinsi ve katkılanan nadir toprak elementi miktarındaki değişikler temel alınarak en iyi lüminesan değerlerini veren ürünü bulmayı kapsamaktadır.

Mikrodalga sentezi metodu için üre kullanılmıştır. Mikrodalgada sentez tamamlandıktan sonra, malzeme 950° C' de iki saat ısıtılmıştır. Mikrodalga destekli sol-jel metodu içinse, sitrik asit ve glisin kullanılmıştır. Jel karışımı elde edildikten sonra, ürün 1200 W'luk mikrodalga fırında 10 dakikada başarılı bir şekilde sentezlenmiştir. Bu yöntem için de 950° C' de iki saat ısıtma uygulanmıştır.

X Işınları toz kırınımı (XRD) metodu malzemenin karakterizasyonu için kullanılmıştır. Katkılı ve saf ürünün morfolojik çalışması Taramalı Elektron Mikroskobu (SEM) ve Geçirimli Elektron Mikroskobu (TEM) kullanılarak tamamlanmıştır. Sentezlenen maddelerin uzay grubu *Pnma*, kristal sistemi ortorombik ve birim hücre parametreleri ise a= 5.876(1) Å, b= 5.105(9) Å c= 8.252(1) Å olarak bulunmuştur. Ayrıca, bağ yapısı ve bantları tanımlayabilmek adına FT-IR spektrometresi analizleri gerçekleştirilmiştir. Lüminesan çalışmaları da Floresans spektrometrisi kullanılarak en iyi emisyon geçiş yoğunluklarını bulabilmek adına gerçekleştirilmiştir.

XRD analizleri lantan ortoborat'ların başarılı bir şekilde sentezlendiğini ispatlamaktadır. SEM görüntüleri lantan ortoborat partiküllerinin gruplaştığını ve

düzensiz bir yapısı olduğunu göstermiştir. Üç farklı yakıt kullanaraktan sentezlenen ürünlerin farklı tanecik boyutlarının olduğu gözlenmiştir. FT-IR spektrometresinde tipik $LaBO_3$ bantları gözlenmiştir bu da ürünlerin başarılı olarak sentezlendiğini destekler. Lüminesan çalışmalarında da en yoğun geçişlerin üre yakıtıyla sentezlenen malzemeden geldiği görülmüştür.

Anahtar Sözcükler: Lantan ortoborat, evropiyum, disprosyum, terbiyum, lüminesan, sitrik asit, üre, glisin, mikrodalga-destekli, sol-jel.

to my family...

ACKNOWLEDGEMENTS

I owe Assoc. Prof. Dr. Ayşen Yılmaz and Assoc. Prof. Dr. Okan Esentürk debt of gratitude for their kind supervision, encouragement, guidance and criticism.

I would like to express my sincere thanks to Prof. Dr. Ahmet M. Önal and Prof. Dr. Mürvet Volkan for their assistance by letting me operate their laboratory equipment during the experimental stages of the thesis. I am also appreciative to Ezgi Altın, Gamze Gezer and Eda Karaaslan, for their incalculable helps and sharing a peaceful and efficient working environment in the laboratory.

I wish to express my thanks to my colleagues for their assistance and guidance during this research.

I offer my sincerest thanks to my beloved family for their encouragement, love and motivation by all means.

TABLE OF CONTENTS

LIST OF TABLES

TABLES

LIST OF FIGURES

FIGURES

CHAPTER 1

INTRODUCTION

1.1 Borates

Boron is a second period, third group element having a semi-metallic property with an atomic number of 5. Boron usually occurs in the nature mostly as borate minerals and borosilicate, in the nature, 230 borate minerals are known as a source of boron [1]. Despite of the fact that boron is a rare element in the earth crust, because of its solubility in water it can be found in some regions abundantly. Boron is unable to occur in the nature as a free element due to their unsteady nature in the elemental form. Because boron atoms tend to form compounds with the other elements, commercial boron is very tough to be purified. Nevertheless, there are major distributors of boron mineral deposits in the world such as, South West USA, Mojave Desert, Turkey and Argentina [2].

Boron minerals are natural compounds haing various amounts of boron oxide (B_2O_3) in their structure. It is known that there are over 230 boron minerals in nature. Tincal ($Na_2B_4O_7x10H_2O$), colemanite ($CaB_3O_4(OH)_3xH_2O$), kernite ($Na_2B_4O_6(OH)_2x3H_2O$) and ulexite ($NaCaB_5O_6(OH)_6x5(H_2O)$) are most abundant minerals in the boron reserves throughout the world and Turkey. These boron minerals are generally sodium, calcium and sodium together with calcium based boron compounds [3]. The total boron world reserves are around 918 million tons on B_2O_3 basis with the subsequent shares given in Table 1.

Table 1: World B_2O_3 Reserves [2]

Country	**B_2O_3 Total Reserve (million tons)**
Turkey	563
Russia	100
USA	80
Chile	41
China	36
Mexico	27
Peru	22
Bolivia	19
Kazakhstan	15
Argentina	9
Serbia	3
Others	3
General	918

Borates have various sorts of applications on different basis depending on the source. Today, 43% of the borate applications are based on glass industry. An illustration is shown in Fig. 1 to demonstrate the applications. Followed areas can be lined up as detergent, agricultural and glaze areas [4]. Moreover, it has been noticed that borates provide a long lasting, odorless as well as low acute toxicity pesticide in agricultural usage [5]. A supplementary detailed demonstration has been shown in Fig. 1 to illuminate the applications in detail.

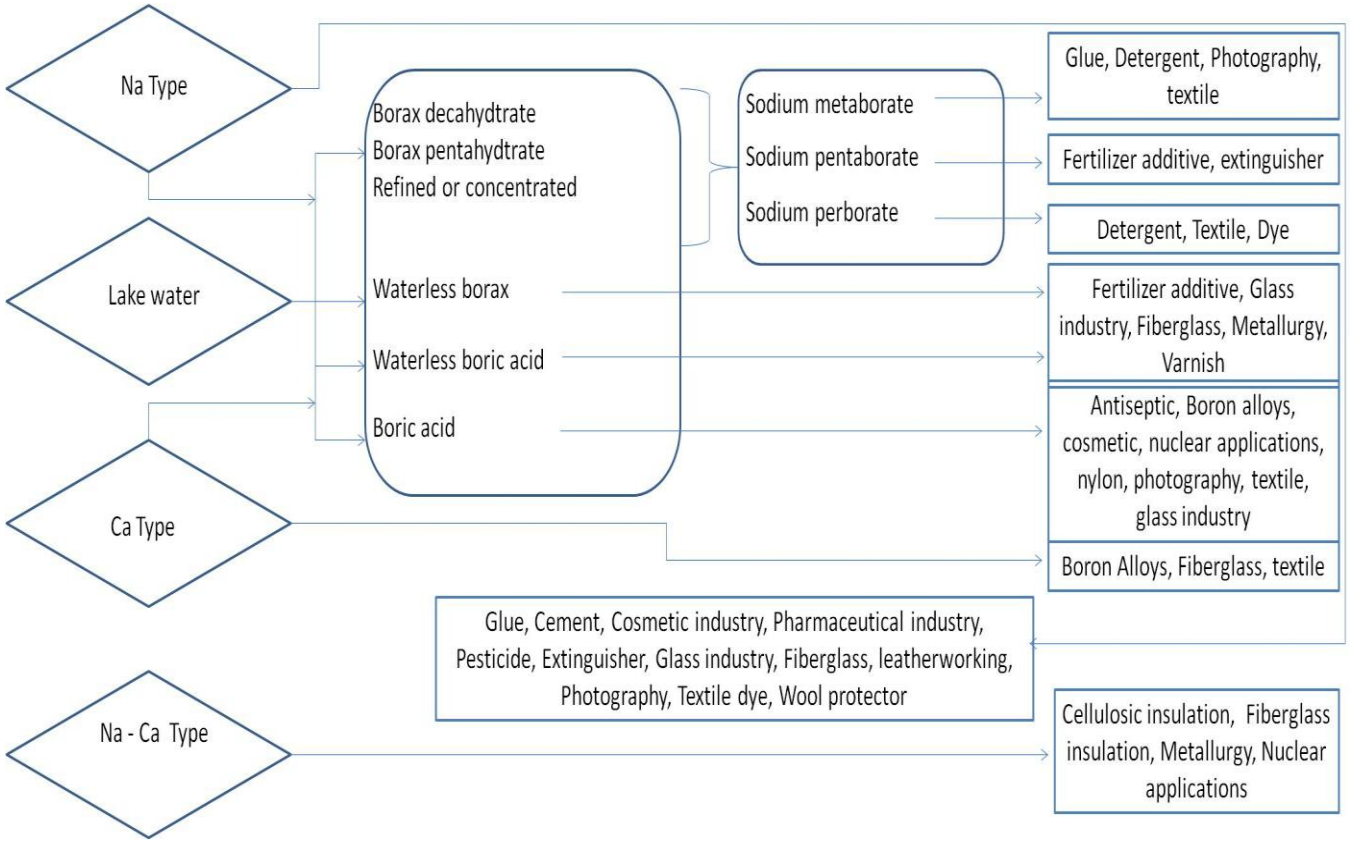

Figure 1: Usage of Boron products and the sectors utilizing boron [6]

1.2 Luminescence and Selection Rules

"*A history of luminescence from the earliest times until 1900*" is a remarkable book, which is written by Harvey Newton in 1957, about the early history of Luminescence. The preface starts with word "*luminescenz*" which was first used in history by Eilhardt Wiederman, a German physicist and historian. He figured out that, with an increase in temperature, some liquids and solids emit radiation. The awareness of luminescent materials starts incredibly long time ago. It is believed that Neanderthal (~ 200, 000 – 28, 000 years ago) knew of many luminescent creatures one of which is a luminous bacterium [7]. In 1933, Alexander Jablonski has published his works in Nature magazine and simply made his name immortal. He studied the efficiency of anti-stokes Fluorescence in dyes and later on, his famous diagram was drawn. If a molecule is exposed to certain amount of energy, it is excited to a higher electronic energy level [8]. Figure 2 illustrates the fundamental pathways of Jablonski diagram. According to diagram, if a molecule is absorbed by any kind of energy, it should dissipate this energy through a certain corridor according to the energy applied. These pathways can be Fluorescence, Phosphorescence, Internal conversion or Intersystem crossing.

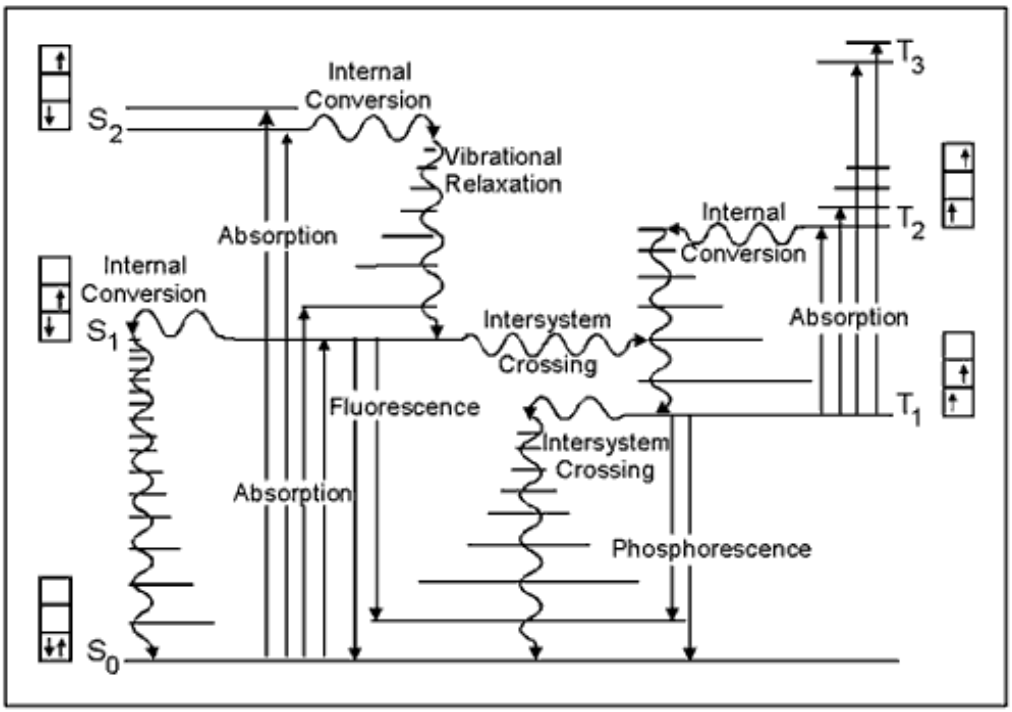

Figure 2: The basics of Jablonski diagram [9]

Another diagram that is based on the interaction coordinates and potential energy diagram is called Franck-Condon energy level diagram which is demonstrated in Figure 3. The diagram illustrates the ground state and the first excited singlet state, S_0 and S_1, respectively. In the Franck-Condon diagram, the parallel lines refer to each energy level. So the arrows in between these horizontal lines indicate the transitions between the energy levels [9]. The energy of photon that is emitted during relaxation from S_1 to S_0 can be calculated.

$$E = h\nu = h\frac{c}{\lambda}$$

E expresses the energy, h is Planck's constant, c is speed of light, v refers to frequency and λ stands for the wavelength.

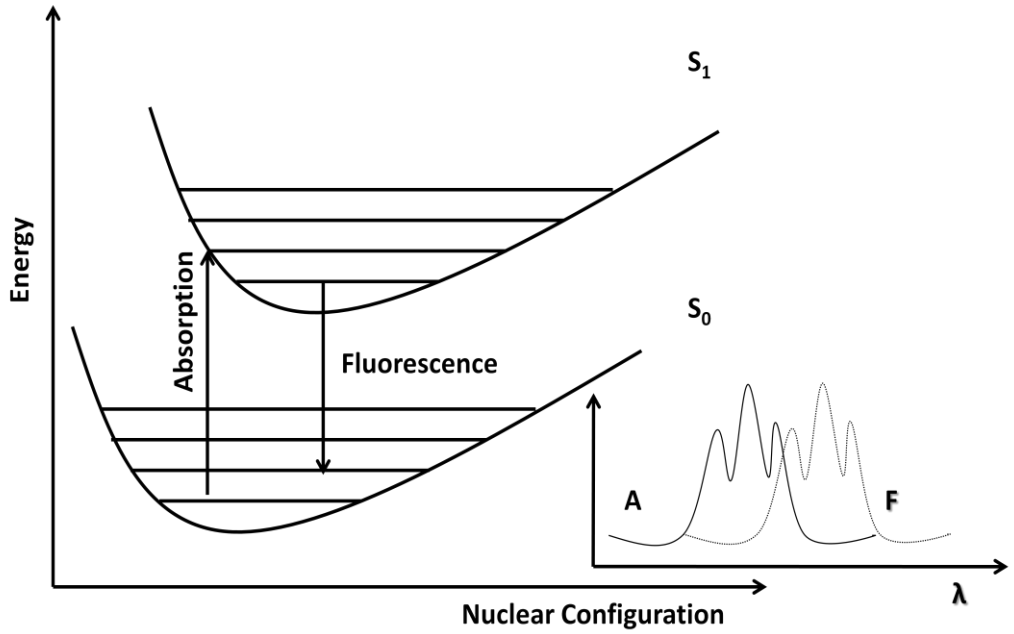

Figure 3: Franck-Condon Energy Level Diagram [9]

All the electronic transitions must strictly obey selection rules which can be summarized as spin selection rule and Laporte selection rule. According to spin selection rule, the transition may take place from singlet to singlet or triplet to triplet states or quartet to quartet etc. and a change in spin multiplicity is forbidden, $\Delta S = 0$. According to Laporte selection rule, there has to be a change in parity. The allowed transitions are *g* to *u* or *u* to *g*. Forbidden transitions are from *g* to *g* or from *u* to *u*, as a result, the Laporte selection rule can be shortened up to $\Delta l = \pm 1$ [10].

1.3 Rare Earth Elements, Their Functions, IR Investigations and Luminescence Properties

Rare Earth elements (REE) are the set of seventeen elements in the periodic table. They include fifteen lanthanide elements with atomic numbers varying between 57 and 71, as well as yttrium with atomic number of 39. They were mostly isolated in the late 18^{th} 19^{th} centuries as oxides. Rare earth elements which are known to be very reactive are finally discovered in the 20^{th} century. The lanthanide elements are split into two parts; the light rare earth (LRRE) elements are from lanthanum through europium and the heavy rare earth elements (HRRE) are from gadolinium through lutetium [11].

In the past four decades, the applications and the usage of rare earth elements have grown considerably. The application area of rare earth elements is very wide despite the rare sources and lack of rich ores in the earth crust. Basically, the essential areas of the main applications can be highlighted as nuclear, metallurgical, catalytic, electrical, magnetic and optical industries. As there are a diverse number of branches that utilizes the valuable properties of REE, the application range is particularly wide such as lighter flints, glass polishing, phosphors, lasers, magnets, batteries, magnetic refrigeration, high temperature superconductivity, safe storage and transport of hydrogen for a post-hydrocarbon economy [12].

For the IR study of the $LaBO_3$ particle, there are very consistent results in the literature [30, 31]. A typical IR spectrum of $LaBO_3$ has a band at 1400 cm^{-1} which indicates BO_3 group. Likewise, bands at 900 and 1050 cm^{-1} is due to tetrahedral borate group BO_4. At 1250 cm^{-1}, the v3 (asymmetric stretching) bands are seen around. The v1 (symmetric stretching) and v2 (out of plane bending) bands are respectively seen around 940, 708 cm^{-1}, while v4 (in plane bending) band gives

rise at 590 and 610 cm^{-1} [32]. Moreover, BO_4 feature on FT-IR spectrum at 1050 cm^{-1} is corresponded to ring formation for the $LaBO_3$ powders [32].

Efficient luminescence properties of REE are a further noteworthy research topic. In the last three decades luminescence properties of REE has taken such a remarkable place in study. Table 2 exemplifies the luminescence applications of REE with respect to their critical features [13].

Many groups have carried out an assortment of studies [14 - 17] on luminescence properties of REE in a mixture of type of compounds. M. Gafta *et al*. have studied the laser induced luminescence of REE and reported the relative excitations and transitions in table 3 [14]. For Ce^{3+}, the observed transitions are from $^2D \rightarrow {}^2F$ at 266 nm excitation. For Pr^{3+}, Sm^{3+}, Eu^{3+}, Dy^{3+}, Ho^{3+} and $^{3+}$, the approximate excitation is around 337 nm. Pr^{3+} has $P_0 \rightarrow$ H transitions, as well as $D_2 \rightarrow$ H transitions. The observed transitions for Sm^{3+} are $G_{5/2} \rightarrow$ H transitions. Eu^{3+} shows $D_0 \rightarrow$ F transitions. Dy^{3+} has F → H transitions while Ho^{3+} has S → I and F → I transitions. Er^{3+} undergoes S → I transitions whereas Tm^{3+} goes through I → H, D → H and G → H transitions. Gd^{3+} shows P → S transitions at 266 nm. Similar to Gd^{3+}, Tb^{3+} has the same excitation at 266nm for D → F transitions. Conversely, these emission wavelengths can show a discrepancy with respect to different types of matrixes [18].

Table 2: Luminescence applications of Rare Earth Elements [13]

Application	RE used	Excitation	Critical Features
Lighting	Eu^{2+}, Eu^{3+}, Tb^{3+}	UV-radiation	Chemical stability, UV-absorption
TV/ cathode ray tubes	Eu^{2+}, Eu^{3+}	Electrons	Chemical stability, fast luminescence
Scintillators	Ce^{3+}	g-/X-rays	Absorption of radiation, fast luminescence
Electroluminescence	Ce^{3+}, Tb^{3+}, Eu^{3+}	Electric field	Energy conversion, fast luminescence
IR-vis conversion	Yb^{3+}, Er^{3+}, Tm^{3+}, Ho^{3+}	IR-radiation	Energy transfer
Photostimulated luminescence	Ce^{3+}, Eu^{2+}	X-rays	Trap formation, depth of traps
Laser	Nd^{3+}, Yb^{3+}	UV-radiation	Chemical stability, laser action
Fiber optics	Er3+	IR-radiation	Transparency
Persistent Luminescence	Eu^{2+}; Nd^{3+}/Dy^{3+}	Thermal energy	Depth of traps

Table 3: Transitions and excitation wavelengths of REE by laser induced luminescence

Center	λ_{lum} (nm)	λ_{ex} (nm)	τ (μs)	Transition
Ce^{3+}	355	266	2×10^{-2}	$^2D-^2F$
Pr^{3+}	489	337	1	$^1P_0\rightarrow{}^3H_4$
	596		10	$^1D_2\rightarrow{}^3H_4$
	621		10	$^1D_2\rightarrow{}^3H_4$
Sm^{3+}	565	337	550	$^4G_{5/2}\rightarrow{}^6H_{5/2}$
	601,612		550	$^4G_{5/2}\rightarrow{}^6H_{7/2}$
	647		550	$^4G_{5/2}\rightarrow{}^6H_{9/2}$
Eu^{3+}	596	337	1500	$^5D_0\rightarrow{}^7F_1$
	616		50	$^5D_0\rightarrow{}^7F_2$
	654		1500	$^5D_0\rightarrow{}^7F_3$
	702		1500	$^5D_0\rightarrow{}^7F_4$
	707		1500	$^5D_0\rightarrow{}^7F_4$
Gd^{3+}	312	266	2500	$^6P\rightarrow{}^8S_{7/2}$
Tb^{3+}	383	266	325	$^5D_3\rightarrow{}^7F_6$
	415		325	$^5D_3\rightarrow{}^7F_5$
	437		325	$^5D_3\rightarrow{}^7F_4$
	489		2400	$^5D_4\rightarrow{}^7F_6$
	548		2400	$^5D_4\rightarrow{}^7F_5$
Dy^{3+}	478	337	120	$^4F_{9/2}\rightarrow{}^6H_{15/2}$
	575		120	$^4F_{9/2}\rightarrow{}^6H_{13/2}$
Ho^{3+}	549	337	1	$^5S_2\rightarrow{}^5I_8$
	665		1	$^5F_3\rightarrow{}^5I_7$
Er^{3+}	549	337	10	$^4S_{3/2}\rightarrow{}^4I_{15/2}$
	559		10	$^4S_{3/2}\rightarrow{}^4I_{15/2}$
Tm^{3+}	289	266	15	$^1I_6\rightarrow{}^3H_4$
	347		15	$^1I_6\rightarrow{}^3H_6$
	458		5	$^1D_2\rightarrow{}^3H_4$
	483		120	$^1G_4\rightarrow{}^3H_6$

K. Annapurna *et al.* studied the emission properties of Eu^{3+} ions with different excitations and realized that the sample can be excited at diverse wavelengths

on the other hand; the intensity fluctuates with regard to the alteration in wavelength. For Eu^{3+}, the main emission peak is at 610 nm, which is for $^5D_0 \rightarrow 7F_2$ transition, gives six excitations at 393 nm, 232nm, 382 nm, 362 nm, 320 nm and 413 nm [16]. Figure 4 shows the illustration of Eu^{3+} at different wavelengths.

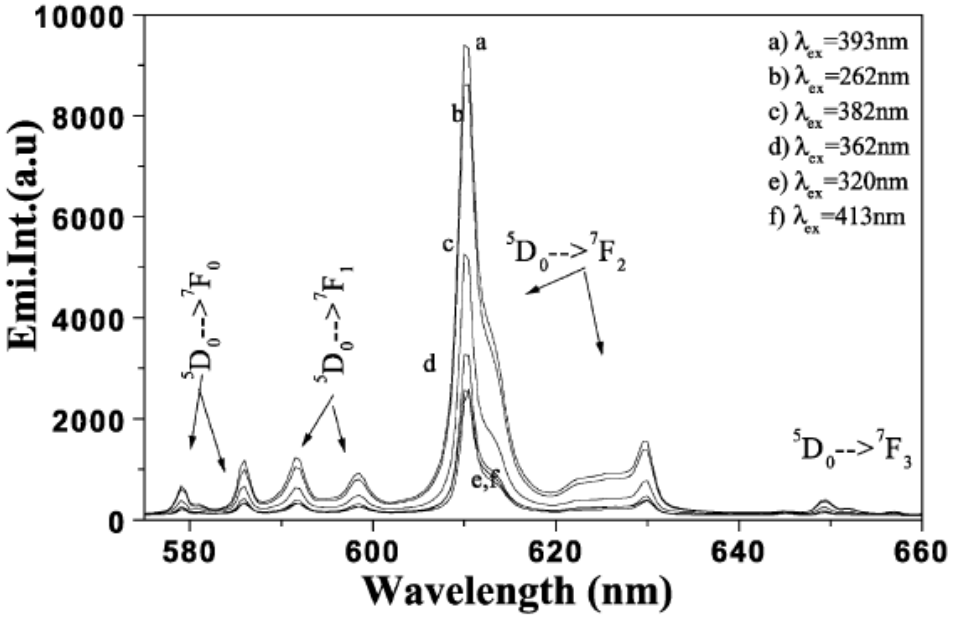

Figure 4: Emission of Eu^{3+} at different wavelengths [16].

As stated above, the emission of Eu^{3+} is mostly from $^5D_0$ state. M. A. Zaitoun has studied concentration quenching of Eu^{3+} and quenching by water. To eliminate the quenching problem there are two well known ways [15]. It is either the isolation of the metal ion from deactivated complex or, doping the REE in a solid matrix [19 - 21]. Figure 5 visualizes the energy diagram for Eu^{3+} transitions [15].

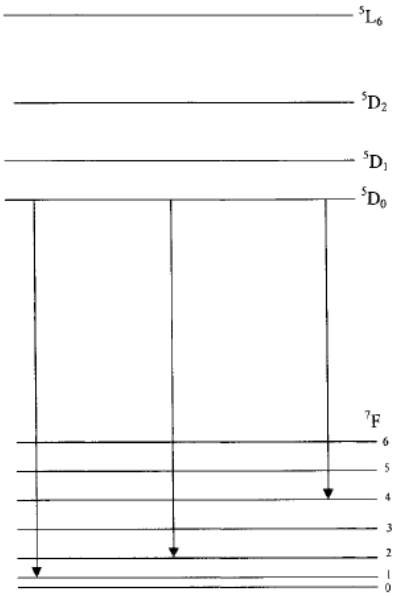

Figure 5: Energy level diagram for Eu^{3+} transitions [15].

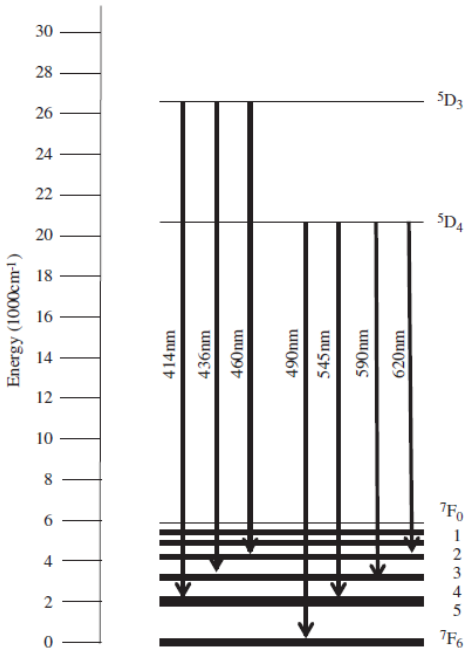

Figure 6: Energy diagram of terbium between 400 nm and 600 nm [27].

Figure 6 illustrates partial energy diagram of Tb from 400 to 600 nm. the major emission is from $^5D_4$. The most intensive and the strongest transition belongs to $^5D_4 \rightarrow {}^7F_5$, which produces the green color [22]. It has been known that Terbium

is a fine host lattices that are used in flat displays, mercury free fluorescent tubes, as well as plasma display panels [23 - 25]. R. Velchuri *et al.* have recently studied some REE orthoborate synthesis and showed their emissions. They approved that the products tend to form different structure by changing the RE. For instance, pure $TbBO_3$ and $DyBO_3$ have vaterite structure; $LaBO_3$ has aragonite structure no matter which RE is doped on it [26]. The luminescence studies of $LaBO_3$:Tb were done by changing the amount of doped Tb in an order of 2.5, 5, 7,5 and 10 mol %. They found the maximum absorption at 378 nm by taking the excitation spectra under the emission wavelength of 543 nm [26]. The emission spectrum of $LaBO_3$:Tb at 378 nm is shown in Figure 7. According to the luminescence studies, they detected the best emission intensity for $LaBO_3$:Tb as 5 mol %. Zhang *et al.* made an analogous class of study of Eu and Tb with 1,10-phenanthroline in-situ synthesized in a silica matrix. They found different excitation numbers for the same doping material in different matrixes. Interestingly, the maximum emissions are observed roughly in the same wavelength (544 nm for Tb, 612 nm for Eu), no matter what the excitation wavelength is chosen [27].

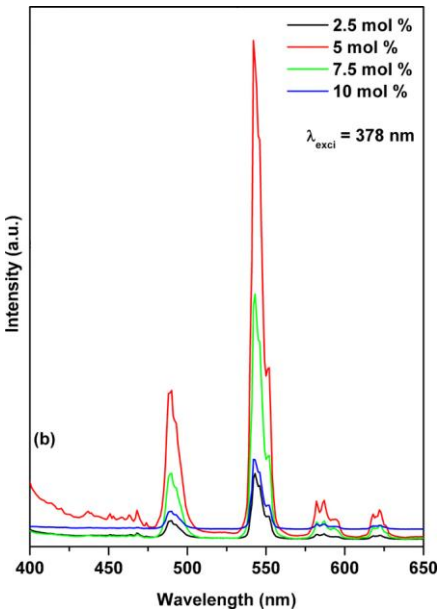

Figure 7: Emission spectra of $LaBO_3$:Tb at 378 nm by changing terbium amount [26]

Because Dy has the capacity to emit the light in diverse regions, it has frequently been used as white light source despite of the fact that the $^4F_{9/2} \rightarrow {}^6H_{13/2}$ yellow transition is superior to white. The most intensive emission is usually seen at 477nm for Dy or Dy doped matrixes [28]. Figure 8 demonstrates the reason why $^4F_{9/2}$ level is highly populated. Because of the small gaps right above 21000 cm^{-1}, non radiative relaxation results all the excited electrons to relax at $^4F_{9/2}$ level from which the strong blue and yellow transitions occur. Despite the quenching luminescence effect of doped Tb after a certain mol %, C. Madhukar Reddy *et al.* have recently found that, increasing the Dy dosage has an rising effect on luminescence intensity strength of the material [27]. At 386 nm excitation, Reddy *et al.* found three emissions of $^4F_{9/2} \rightarrow {}^6H_{15/2}$, $^6H_{13/2}$ and $^6H_{11/2}$ at 484, 576 and 664 nm, respectively. They found the $^4F_{9/2} \rightarrow {}^6H_{11/2}$ transition (red) the less intense while the other two transitions (blue and yellow) are reasonably stronger [29].

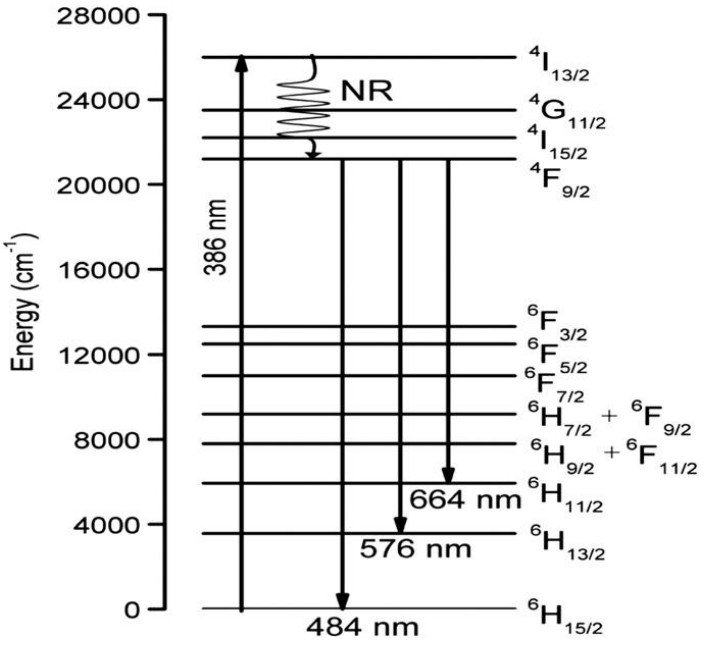

Figure 8: Energy level diagram for dysprosium at 386 nm [29]

1.4 Crystal Structure of $LaBO_3$

In 1961 when Levin *et al.* published their studies of the simplest Lanthanide orthoborate, $LaBO_3$, they proposed that; conditional on the rare earth, the structures of the rare earth borates are immensely linked with the three crystalline forms of $CaCO_3$, that are aragonite, vaterite and calcite types [33]. The light RE orthoborates display the aragonite type structure and the heavy elements of the Lanthanide group demonstrate vaterite type structure. Nevertheless, today five crystal structures (based on previously described crystalline forms) of the RE orthoborates are known: the hexagonal vaterite type (space group P63/m, No. 176) [30, 34], the orthorhombic aragonite type (Pnam, No. 62) [30, 35], the rhombohedral vaterite type (R32, No. 155) [36], and the rhombohedral calcite type (R3c, No. 161) [37] and monoclinic pseudowollatonite type (C2/c, No.15) [38, 39]. It is very important to notice that BO_3 triangles are different from the standard $CaCO_3$ vaterite [38]. $(Y_{0.92}Er_{0.08})BO_3$ has a C2/c space symmetry with the cell constants *a*=12.2019(3) Å, *b*=7.0671(2) Å, *c*=9.3424(2) Å, and *β*=115.347(1) °. Lately, Huppertz *et al.* found that π-$ErBO_3$ has a monoclinic pseudowollastonite-type structure with C2/c space symmetry with the lattice constants a=11.284(2) Å, b=6.526(2) Å, c=9.540(2) Å, and β=112.8(1) ° [38, 39]. Figure 9 shows the aragonite type $LaBO_3$ structure where that blue colored La atom is surrounded by orange colored trigonal BO_3 structure.

Table 4: Methods for fine ceramic powders [41]

1) Mechanical (powder mixing)	a) Ball milling b) Attrition milling c) Vibration milling
2) Thermal decomposition	a) Heating (evaporation) b) Spray drying c) Flame spraying d) Plasma spraying e) Vapour phase (CVD) f) Freeze drying (cryochemical) g) Hot kerosene drying h) Hot petroleum drying i) Combustion j) Laser beam k) Electron beam l) Sputtering
3) Precipitation or hydrolysis	a) Neutralization and precipitation b) Homogeneous precipitation c) Coprecipitation d) Salts solution e) Alkoxides f) Sol-gel
4) Hydrothermal	a) Precipitation (coprecipitation) b) Crystallization c) Decomposition d) Oxidation e) Synthesis f) Electrochemical g) Mechanochemical h) RESA (reactive electrode submerged arc)
Hydrothermal + microwave Hydrothermal + ultrasonic	
5) Melting and rapid quenching	

These entire synthesis routes have different source of energy with lots of variables. Although there are plenty of synthesis pathways, the most important aim is to find most efficient technique with the lowest energy utilization. In many studies [42, 43], it has been revealed that the synthesis route and the type of the chelating agent have a direct effect on the size, structure and the optical

activity of the produced compound. S. D Han et al. reported that increasing the annealing temperature from 500 °C to 1100 °C has an increasing effect on luminescence property of the Dy^{+3} doped compound [*44*]. A. K. Singh et al. studied the effect of capping agents on luminescence and optical activities; they found that thioglycerol causes the highest intensity in luminescence [42]. In the following part some of the most used and essential synthesis routes are expressed.

Combustion synthesis is also an effective and usually low cost method for the production of diverse numbers of industrial materials. Especially for the synthesis of nanomaterials, combustion synthesis is one of the favorite methods [46]. However one of the main disadvantages of combustion synthesis is relatively high level of porosity. This drawback is overcome by TiO_2 which reacts with carbons. Introducing liquid aluminum in igniting temperature infiltrates the porous matrix. On the other hand, overcoming of porous matrix possesses assured limitations concerning the penetration of the liquid of the metal into the porous ceramic matrix and this eventually causes difficulties in sustaining a stable propagation of the combustion reaction [47].

Hydrothermal synthesis basically includes crystallizing substances with high temperature aqueous solutions at high vapor pressures in high pressure “autoclaves” known as “bombs”. The most important advantage of this method is to initiate crystals generating crystalline phases which are unstable at the melting points. The disadvantages of hydrothermal synthesis are inability of observing the crystal initiation and being very expensive “bombs” [18]. Another difficulty observed is to handle the autoclaves. Should it is not carefully and tightly closed, during the synthesis some explosion may occur or the products will be lost.

Liu *et al.*, demonstrated the advantages of high temperature synthesis over low temperature synthesis [49]. They found that, high temperature synthesis is of use to get high cross linking degree for the products. This ultimately results in the development in the thermal and mechanical stabilities of the product [49]. Similar to combustion synthesis, one drawback of high temperature synthesis is the high porosity and certainly the high energy consumption [50].

Advantages of sol-gel process can be counted as followings: permitting of organic-inorganic materials that do not exist naturally. Additionally, having very pure products, low energy requirements association of the solid colloidal state with a liquid medium, as well as the ability of controlling the kinetics of other materials at low temperature are other advantages. However, one of the biggest limitations of solvent process is the high cost of the precursors especially for alkoxides. However with relatively cheap precursors, it presents many sound benefits [51].

Microwave assisted synthesis method has various valuable advantages in synthesis such as good reaction acceleration, yield improvement, enhanced physicochemical properties and the evolvement of new material phases [45]. For almost all the synthesis there is a need of fuel which should initiate the reaction. Depending on the preferred assets of the product, specific fuels are chosen in line with the desired property. These fuels can be citric acid, glycine, urea, hydrazine, polyethylene glycol, alanine, carbohydrazide etc [53]. Among the other types of fuels, citric acid, glycine and urea have the most versatile properties. Table 5 shows the basic properties of these compounds. Mohebbi *et al.*, have studied the synthesis of nano crystalline products by microwave assisted combustion synthesis by changing the type of the fuels. They found out

that glycine results in high combustion heat, less residual carbon and low cost [54]. Riahi-Noori *et al.*, found that using citric acid may bring the formation temperature to a lower degree because the crystalline size is smaller compared to others and it can form a homogenous gel during the synthesis procedure [55]. Li *et al.*, have also compared the effects of using different fuels and found that the products synthesized by urea gives more intensive peaks in XRD. They also found that, although the product is synthesized successively and proven by XRD, there can be seen some variations in the morphology depending on the type of the fuel [53].

Studies for the changes in the emission properties with respect to the type of the fuels have been recently performed intensively [56-59]. Bacalski *et al.*, and Gomes *et al.*, found that products synthesized by high ratio urea gives the most intensive emission signals compared to others [57,59]. Wun et al., have compared the effects of citric acid, glycine and urea on Europium-Doped Gadolinium Lutetium Oxide emission. They also found that products synthesized by urea gives rise to the most intensive emission transitions [60].

Table 5: Some properties of Citric acid, Urea and Glycine

	Organic component		
Properties	Critic acid	Urea	Glycine
Structural formula	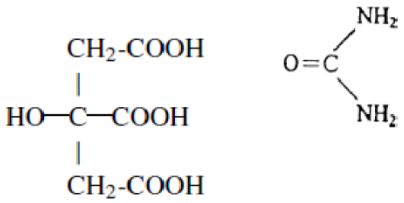		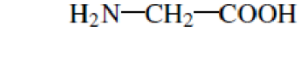
Molecular weight (g/mol)	192.1	60.1	90.1
Heat of combustion (kJ/g)	10.2	10.5	13.0
Decomposition temperature (°C)	175	135	262

CHAPTER 2

MATERIALS AND METHODS

2.1 Materials

There are number of compounds used in this study. Materials other than distilled water were used in powder form. In the following list, the names of solid powders in synthesis and doping of $LaBO_3$ are given in Table 6.

Table 6: List of the materials, their usages and labels

Material Used	Utilization Purpose	Label
$LaCl_3$ x 7 H_2O	$LaBO_3$ production	Fluka ≥98.5%
La_2O_3	$LaBO_3$ production	Aldrich 99.9%)
H_3BO_3	$LaBO_3$ production	Merck
H_2NCH_2COOH (Glycine)	$LaBO_3$ production	Merck
$C_6H_8O_7$ (Citric Acid)	$LaBO_3$ production	Aldrich ≥99.5%
$CO(NH_2)_2$ (Urea)	$LaBO_3$ production	Merck
Eu_2O_3	Doping	Aldrich 99.9%
Dy_2O_3	Doping	Aldrich 99.9%
Tb_4O_7	Doping	Aldrich 99.9%

2.2 Instrumentation

2.2.1 Furnace

All the annealing and further heating have been carried out in air by using Protherm furnace with heating ability up to 1300 °C with a heating control board.

2.2.2. X-Ray Diffractometer

The crystal structures of the pure and doped lanthanum orthoborate compounds were collected by the powder X ray diffraction (XRD) measurements. The XRD data were recorded using Rigaku X-Ray Diffractometer (Model, Miniflex) with CuK_{α} (30kV, 15mA, λ= 1.54051 Å). The 2 theta range adopted for the XRD examinations were determined to be 5° and 80°. The scan speed was adjusted to 1 degree/minute. Diffraction patterns were assigned using Joint Committee on Powder Diffraction Standards (JCPDS) cards supplied by the International Centre for Diffraction Database (ICDD) card numbered 12-0762.

2.2.3 Fourier Transform Infrared Spectrometer (FT-IR)

Attenuated total reflectance-FTIR (ATR-FTIR) spectra were obtained on a Bruker IFS 66/S spectrometer equipped with a ZnSe crystal with the beam incident at an angle of 45°. The samples were analyzed over 500–4000 cm^{-1} range with the resolution of 4 cm^{-1}.

2.2.4 Scanning Electron Microscope (SEM)

Morphologies of the samples were investigated by using a scanning electron microscope (SEM). The analyses were performed using Zeiss SUPRA 50 VP with a magnification between 12 to 900000 and variable pressure between 2 to 133Pa, acceleration voltage between 0.1 to 30 kV.

2.2.5 Transmission Electron Microscope (TEM)

The TEM images were obtained using JEOL JEM 2100F STEM at 200kV. The samples were dissolved in water by the help of Elma S 30 H ultrasonic bath for 10 minutes. After dissolving, a droplet of the solution was released on a grind. Then the grids were taken for the TEM measurement.

2.2.6 Photoluminescence Reader

Photoluminescence was measured by using Varian Cary Eclipse Fluorescence Spectrometer from 580 to 730 nm for Eu, from 450 to 700 for Dy, from 450 to 650 for Tb with 5 nm emission and excitation slits at a rate of 100 nm per minute. The samples are directly determined in solid form without any solvent.

2.3 Experimental Methods

2.3.1 Synthesis of $LaBO_3$

$LaBO_3$ synthesis was carried out with 2 different techniques, microwave assisted sol-gel process with glycine and citric acid and microwave assisted combustion synthesis with urea.

2.3.2 Microwave Assisted Sol-gel Synthesis of $LaBO_3$ With Citric Acid

In this method, citric acid [$LaCl_3x7H_2O$: Citric Acid= 1:1.67 (mol ratio)] was used as a chelating agent. Commercially available $LaCl_3x7H_2O$ and Eu_2O_3 were used as La^{3+} and Eu^{3+} source. Citric acid (0.86g), boric acid (0.166g), Lanthanum chloride

(1.0g) and rare earth oxide (Table 7) were mixed with 15 ml of distilled water in a beaker continuously at 80 °C until the solution became a gel. Afterwards, they were heated in the microwave oven at 1200 W for 10 minutes, and further two hours of heating was applied at 950 °C in a conventional oven. REE were added to the mixture with the other reactants in a mol ratio of 2.5, 5.0 and 7.5 % with respect to $LaBO_3$.

2.3.3 Microwave Assisted Sol-gel Synthesis of $LaBO_3$ With Glycine

The synthesis was done similar to citric acid method, the only difference here was the use of glycine (0.67g) [$LaCl_3x7H_2O$: glycine = 1:3.33 (mol ratio)] as a chelating agent. REE were added to the mixture with the other reactants in a mol ratio of 2.5, 5.0 and 7.5 % with respect to $LaBO_3$.

2.3.4 Microwave - Assisted Synthesis With Urea

In this method, $LaBO_3$ powder crystals were prepared by using urea (0.415g) [La_2O_3: Urea=1:1.33 (mol ratio)] in less energetic microwave - assisted reaction method at 1200 W. Commercially obtained rare earth oxide was added to the mixture of La_2O_3 and H_3BO_3 [La_2O_3: H_3BO_3= 1:2 (mol ratio)] in a ceramic crucible (Table 7). They were grinded together until all the compounds were mixed with each other. Subsequently, the mixture was hold in the microwave oven 10 minutes and further two hours of heating was applied at 950 °C in a conventional oven. REE were added to the mixture with the other reactants in a mol ratio of 2.5, 5.0 7.5 % with respect to $LaBO_3$.Table 7 shows the abbreviations of the all experiments and the simple diagram of the all processes. Below equations show the reactions via citric acid glycine and urea.

$$LaBO_3x7H_2O + H_3BO_3 \xrightarrow{Citric\ Acid\ or\ Glycine} LaBO_3 + HCl + 7H_2O$$

$$La_2O_3 + 2H_3BO_3 \xrightarrow{Urea} 2LaBO_3 + 3H_2O$$

Table 7: Used REE amounts and the abbreviations

Doping Level	Citric acid	Glycine	Urea
2.5 % Eu	citaEu/a 0.012g	glyEu/a 0.012g	ureaEu/a 0.02g
5 % Eu	citaEu/b 0.024g	glyEu/b 0.024g	ureaEu/b 0.04g
7.5 % Eu	citaEu/c 0.036g	glyEu/c 0.036g	ureaEu/c 0.06g
2.5 % Dy	citaDy/a 0.013g	glyDy/a 0.013g	ureaDy/a 0.021g
5 % Dy	citaDy/b 0.025g	glyDy/b 0.025g	ureaDy/b 0.043g
7.5 % Dy	citaDy/c 0.038g	glyDy/c 0.038g	ureaDy/c 0.064g
2.5 % Tb	citaTb/a 0.013g	glyTb/a 0.013g	ureaTb/a 0.022g
5 % Tb	citaTb/b 0.025g	glyTb/b 0.025g	ureaTb/b 0.043g
7.5 % Tb	citaTb/c 0.038g	glyTb/c 0.038g	ureaTb/c 0.065g

CHAPTER 3

RESULTS AND DISCUSSION

3.1 X-Ray Diffraction Patterns

Figure 10, 11 and 12 illustrates the XRD patterns for the $LaBO_3$ with citric acid, glycine and urea precursor, respectively. All the observed patterns of $LaBO_3$ synthesized with three different methods with all types and amount of doping materials belong to same card number (JCPDS no: 12-0762) and have the same h-k-l values (Table 9 - 12). The space group is *Pnma,* and the crystal system is orthorhombic with the unit cell dimensions; a= 5.8761(1) Å, b= 5.10535(9) Å c= 8.252(1) Å. There are some unidentified peaks around 23.0, 29.5 and 34.1 θ degrees seen on $LaBO_3$ synthesized by urea method. These peaks were studied in detail and found out that they are not any of the Lanthanum, Europium, Dysprosium or Terbium including compound peaks. On the other hand, it is a common feature which is seen by other groups working on $LaBO_3$ [52].

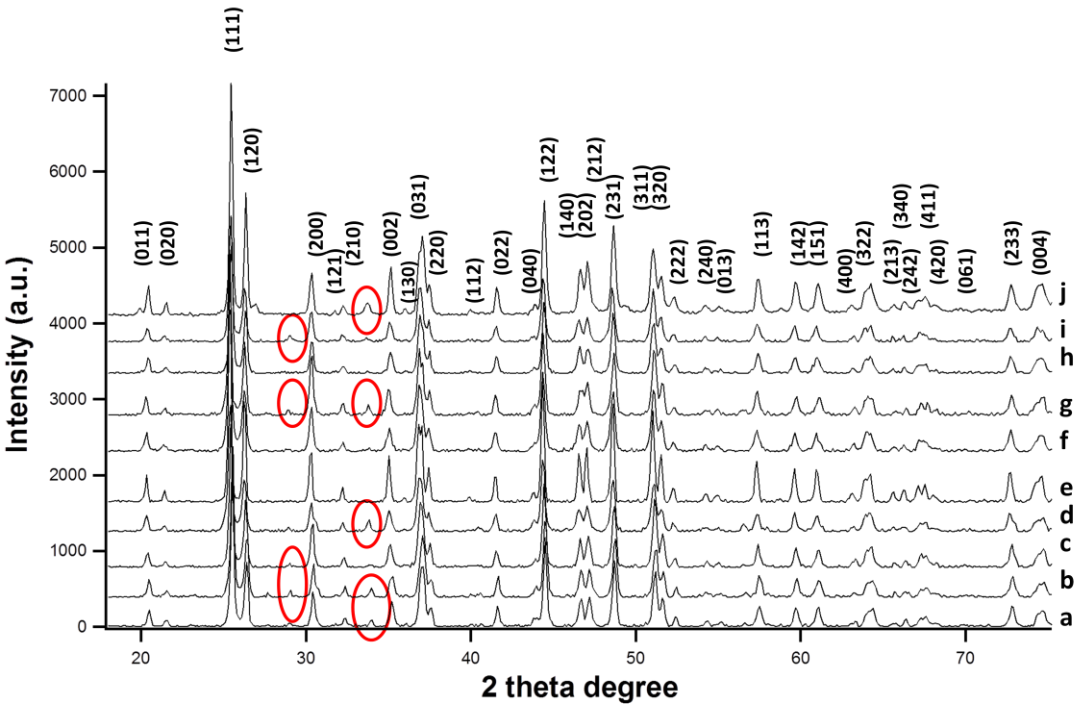

Figure 10: XRD patterns of REE doped $LaBO_3$ with citric acid precursor. **a)** pure $LaBO_3$, **b)** citaEu/a, **c)** citaEu/b, **d)** citaEu/c, **e)** citaDy/a, **f)** citaDy/b, **g)** citaDy/c, **h)** citaTb/a **i)** citaTb/b, **j)** citaTb/c.

Below image on figure 12 also demonstrates the intensive X-Ray Diffraction pattern, taken for around 19 hours, for the terbium doped lanthanum orthoborate between 20-40 degrees. The reason why $LaBO_3$:Tb is chosen for this intensive measurement is because it has all the extra features which do not match with the particular $LaBO_3$ card number. For this intensive measurement it is noticed that the features at 23.0 and 29.5 θ degrees has disappeared. Only remaining unmatched feature is seen at 34.1 degree with a comparatively less intensity. Based on the feature at 34.1 θ degree, another library search has been made to detect the unmatched peak; however, no results have been found.

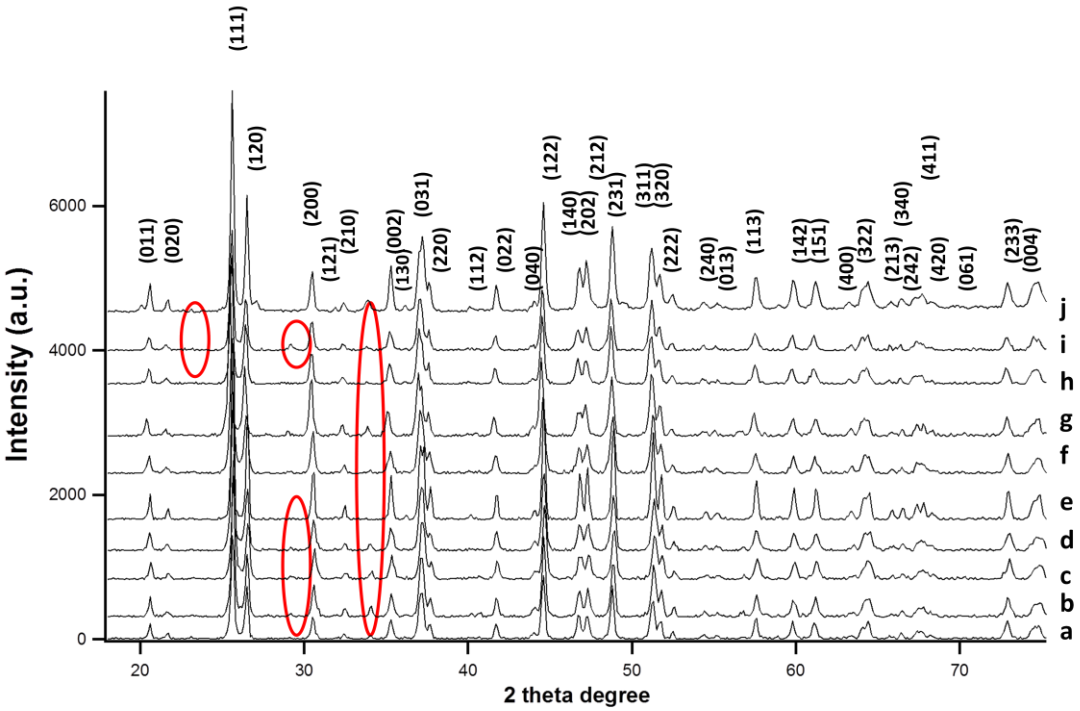

Figure 11: XRD patterns of REE doped $LaBO_3$ with glycine. **a)** pure $LaBO_3$, **b)** glyEu/a, **c)** glyEu/b, **d)** glyEu/c, **e)** glyDy/a, **f)** glyDy/b, **g)** glyDy/c, **h)** glyTb/a **i)** gly/b, **j)** glyTb/c.

In Figure 10, 11 and 12; there is an increasing trend in the intensity of the peaks as a function of doping amount. By increasing the doped REE, the intensity of the peaks is getting thinner and higher. As a comparison, the most intensive peaks belong to the products synthesized by citric acid precursor while the products synthesized by urea have the least intensive XR-D patterns. This suggests that urea product has better crystalline characteristics.

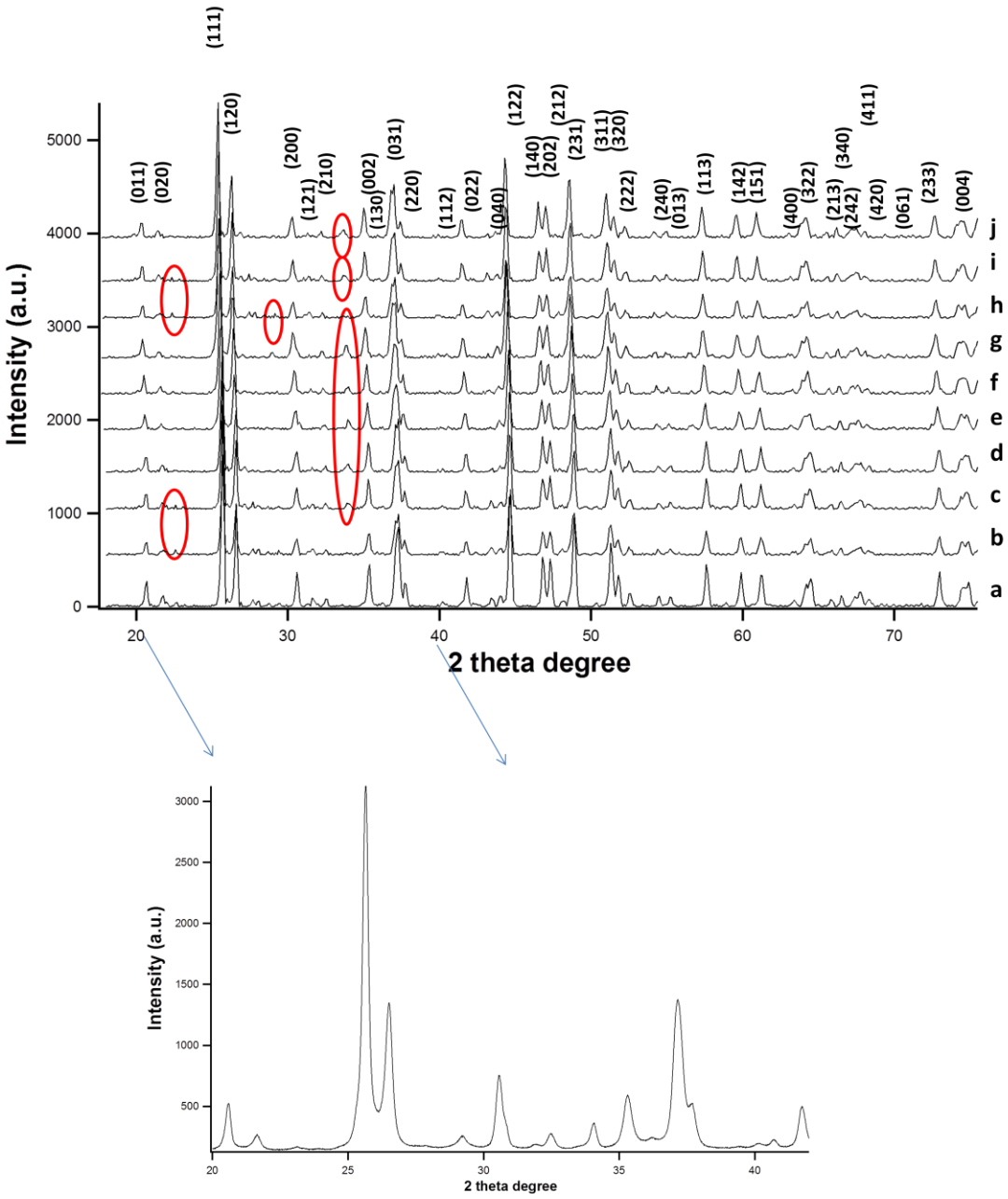

Figure 12: XRD patterns of REE doped $LaBO_3$ with urea. **a)** pure $LaBO_3$, **b)** glyEu/a, **c)** glyEu/b, **d)** glyEu/c, **e)** glyDy/a, **f)** glyDy/b, **g)** glyDy/c, **h)** glyTb/a i) gly/b, **j)** glyTb/c. Below figure shows the detailed XRD patterns between 20-40 degrees.

Scherer formula calculations show that according to XRD results the smallest particles have to belong to the group synthesized by citric acid.

$$\tau = \frac{K\ x\ \lambda}{ß\ cos\theta}$$

τ = Thickness of crystallite

ß = FWHM in radians

***K* =** Shape factor (0.89)

θ = the Bragg angle

λ = X-Ray wavelength

In order to prove the Scherer formula SEM and TEM images were taken which are shown in the next part.

3.2 TEM, SEM and EDX

The SEM images of $LaBO_3:Eu^{3+}$ samples are demonstrated in Figure 13. It revealed that the primary particles of the nano-sized $LaBO_3:Eu^{3+}$ powders are sphere-like in morphology and they tend to agglomerate. It is noticed that $LaBO_3$ synthesized by citric acid precursor has the smallest size among them. When the particle size of $LaBO_3$:Eu particle sizes are compared with respect to type of the fuels, citric acid gives the smallest size. For the pure and Eu doped $LaBO_3$, the increasing order with respect to the size is as followed; citric acid, glycine and urea. Citric acid gives the particle size around ~ 90 – 120 nm for the pure $LaBO_3$

For glycine, it is around ~ 150 – 350 nm for the pure $LaBO_3$ and ~ 700– 1000 nm for pure $LaBO_3$. It is observed that sizes of the REE doped $LaBO_3$ and pure $LaBO_3$ seem roughly the same.

Figure 14 presents the TEM and HRTEM images of $LaBO_3$ by citric acid, glycine and $LaBO_3:Eu^{3+}$ by glycine fuels. The right and left of Fig. 14 exhibit high and low magnification TEM images of the samples, respectively. These images show that particles are not in the uniform size, they are highly crystalline in nano-size, structurally uniform and free from defects and dislocations. The HRTEM image of Fig. 14b inset, $LaBO_3$ prepared by using glycine, demonstrates that a uniform single-crystal structure is available.

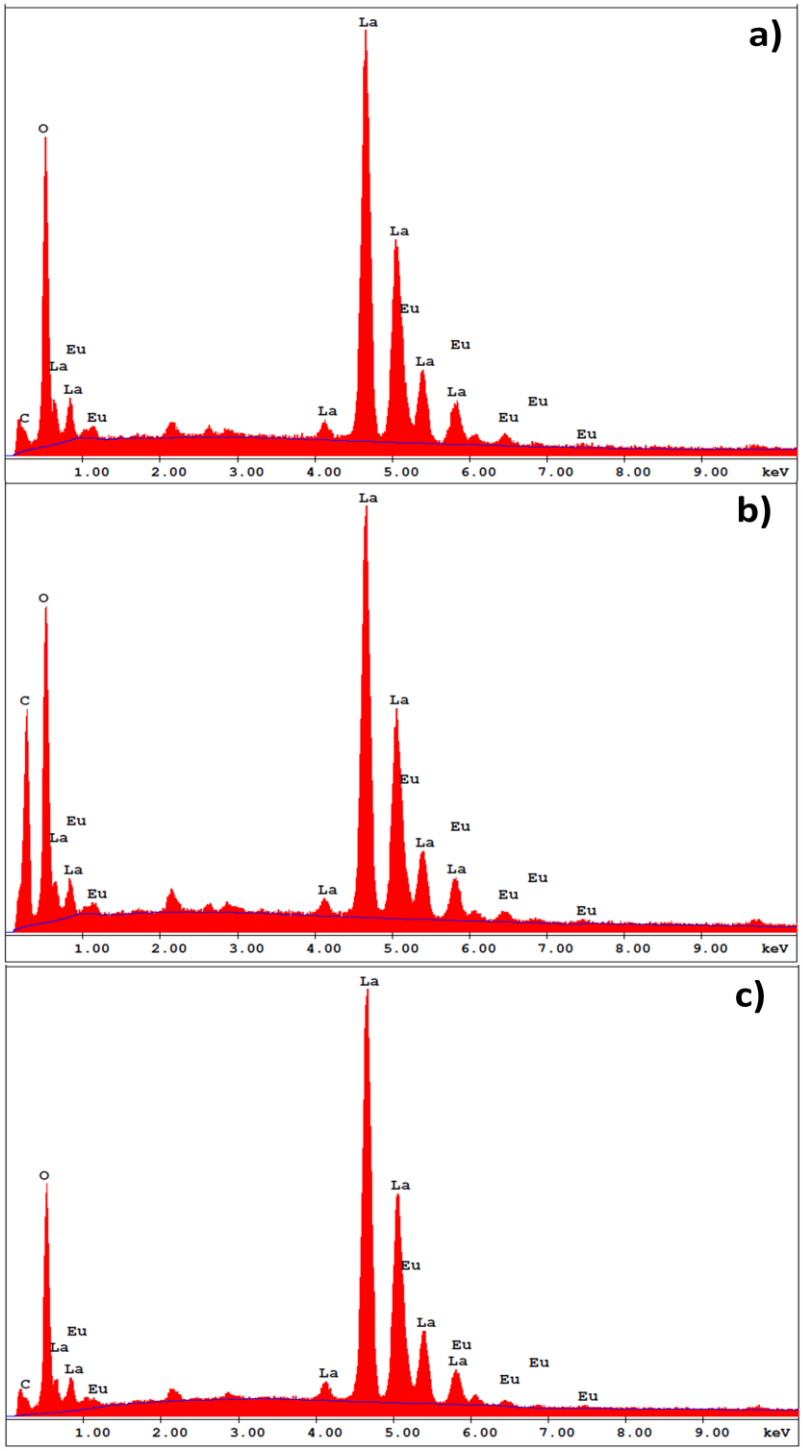

Figure 15: EDX Results for the Eu doped $LaBO_3$ by a) citric acid b) glycine c) urea

3.3 FT-IR Analysis

Figure 16, Figure 17 and Figure 18 demonstrate the FT-IR spectrum of $LaBO_3$ powder synthesized by three different precursors. Each figure illustrates the comparison of pure $LaBO_3$ and REE doped samples with different percentages are compared. First as a qualitative analysis, all the samples from different precursors give rise at the same wavelengths for the specific vibration.

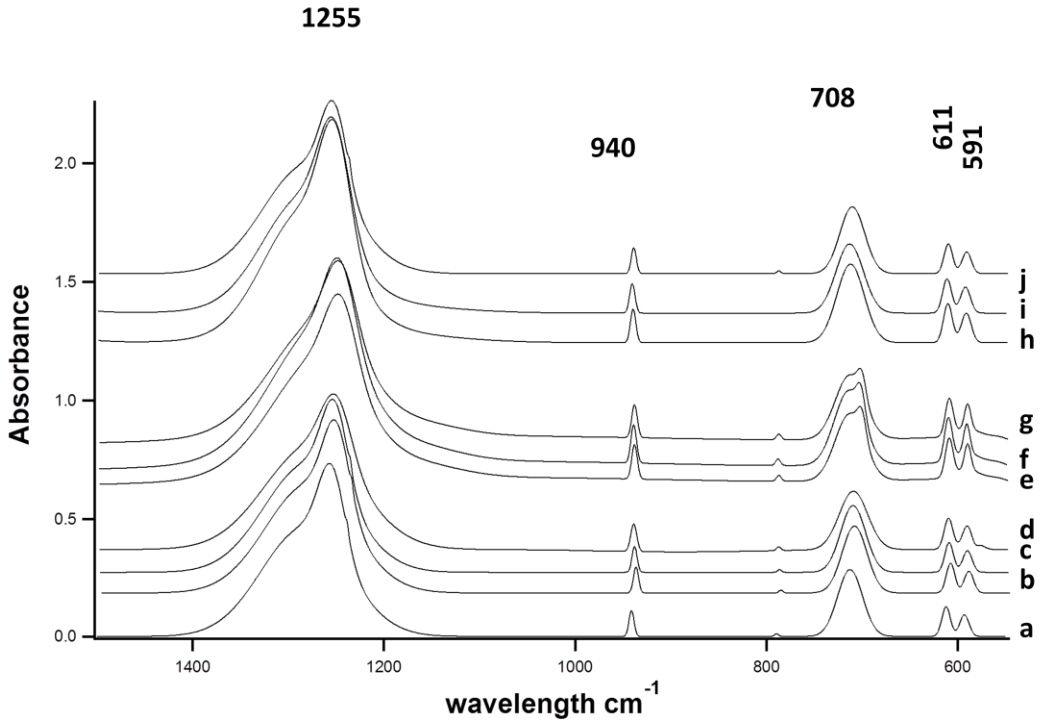

Figure 16: FTIR spectrum of $LaBO_3$ powder with citric acid precursor. a) pure $LaBO_3$, b) 2.5 % $LaBO_3:Eu^{3+}$, c) 5 % $LaBO_3:Eu^{3+}$,d) 7.5 % $LaBO_3:Eu^{3+}$, e) 2.5 % $LaBO_3:Dy^{3+}$, f) 5 % $LaBO_3:Dy^{3+}$, g) 7.5 % $LaBO_3:Dy^{3+}$, h) 2.5 % $LaBO_3:Tb^{3+}$, i) 5 % $LaBO_3:Tb^{3+}$, j) 7.5 % $LaBO_3:Tb^{3+}$.

As a qualitative analysis, the IR absorption peaks between 900 and 1050 cm^{-1} which are typical of those for the tetrahedral borate group BO_4 [30]. The aragonite type $LaBO_3$ was formed in a pure form in these reactions and

therefore its FT-IR spectra show the development of the BO_3^{3-} absorption bands. We have observed characteristic bands for all the compounds; v3 (asymmetric stretching) band at 1255 cm^{-1}, v1 (symmetric stretching) band at 940 cm^{-1}; v2 (out of plane bending) band around 708, 790 cm^{-1}, and v4 (in-plane bending) bands around 591 and 611 cm^{-1} for the $LaBO_3$ and $LaBO_3:Eu^{3+}$ powders. In Figures 16, 17 and 18, there seems to be a variation for the v2 band as we observe that some of the products give two peaks for the v2 band at 708, 790 cm^{-1}, and some of them give only one peak for the v2 band at 708 cm^{-1}. A detailed list of the observed wave numbers for the v1, v2, v3 and v4 bands are given in table 8 and table 13. All things considered, our FTIR results show a good coherence with literature and with our XRD patterns [32].

Table 8: Observed Absorption bands for $LaBO_3$:REE

v1 symmetric stretching	**v2 out of plane bending**	**v3 asymmetric stretching**	**v4 in-plane bending**
940 cm^{-1}	708, 790 cm^{-1}	1255 cm^{-1}	591 , 611 cm^{-1}

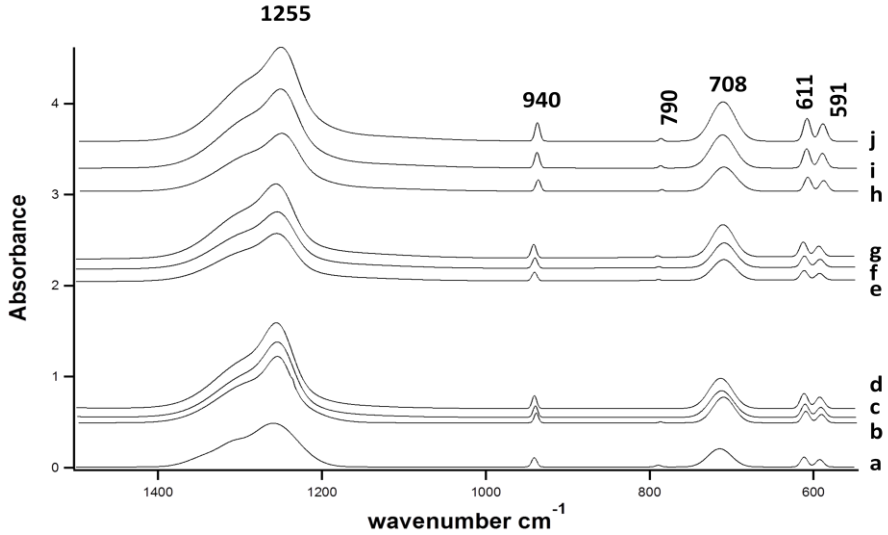

Figure 17: FTIR spectrum of $LaBO_3$ powder with glycine precursor. **a)** pure $LaBO_3$, **b)** 2.5 % $LaBO_3:Eu^{3+}$, **c)** 5 % $LaBO_3:Eu^{3+}$,**d)** 7.5 % $LaBO_3:Eu^{3+}$, **e)** 2.5 % $LaBO_3:Dy^{3+}$, **f)** 5 % $LaBO_3:Dy^{3+}$, **g)** 7.5 % $LaBO_3:Dy^{3+}$, **h)** 2.5 % $LaBO_3:Tb^{3+}$, **i)** 5 % $LaBO_3:Tb^{3+}$, **j)** 7.5 % $LaBO_3:Tb^{3+}$.

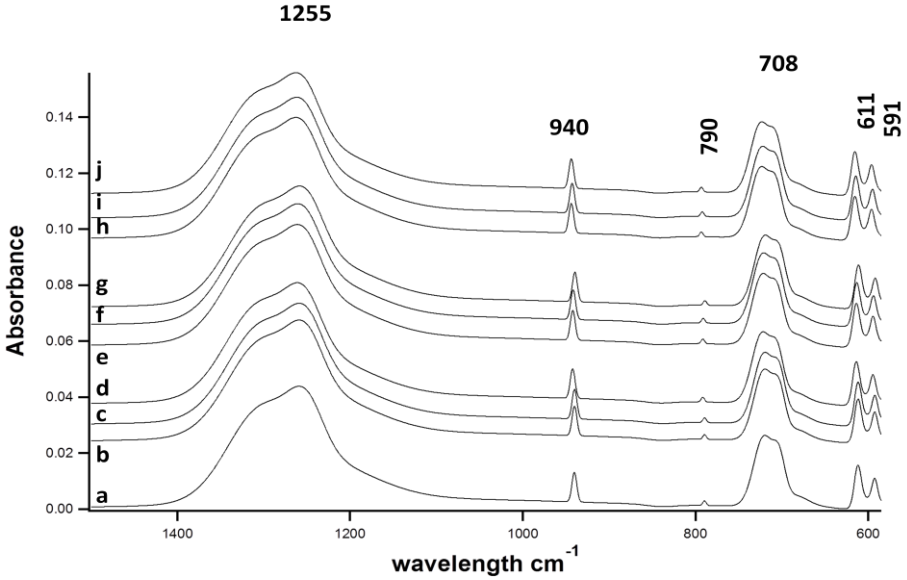

Figure 18: FTIR spectrum of $LaBO_3$ powder with urea precursor. **a)** pure $LaBO_3$, **b)** 2.5 % $LaBO_3:Eu^{3+}$, **c)** 5 % $LaBO_3:Eu^{3+}$,**d)** 7.5 % $LaBO_3:Eu^{3+}$, **e)** 2.5 % $LaBO_3:Dy^{3+}$, **f)** 5 % $LaBO_3:Dy^{3+}$, **g)** 7.5 % $LaBO_3:Dy^{3+}$, **h)** 2.5 % $LaBO_3:Tb^{3+}$, **i)** 5 % $LaBO_3:Tb^{3+}$, **j)** 7.5 % $LaBO_3:Tb^{3+}$.

when the doping amount is 7.5 % of the product. At 2.5 % Eu dosage, the transition at 624 fades and appears as a right shoulder of the transition at 618 nm. When the dosage is 7.5 %, the $^5D_0 \rightarrow {}^7F_2$ transitions at 613 and 618 join to each other to emerge one large peak at 615 nm. For urea, $^5D_0 \rightarrow {}^7F_1$ transition has almost three sites nearly at 588, 590 and 594 nm with 7.5 % of doping. However when the doping amount is 5 %, these three peaks for $^5D_0 \rightarrow {}^7F_1$ transition merge to form one large peak at 591 nm. At lower doping, $^5D_0 \rightarrow {}^7F_1$ transition has 2 peaks at 591 and 595 nm for urea. Unlike the other precursors, urea has $^5D_0 \rightarrow {}^7F_3$ transition. It also gives rise to 6 peaks for the $^5D_0 \rightarrow {}^7F_4$ transition.

Glycine precursor shows also efficient luminescence activity for $LaBO_3$. Unlike the other fuels, it shows $^5D_0 \rightarrow {}^7F_0$ forbidden transition at 584 nm at 7.5 % Eu coverage.

Citric acid gives least intense transitions among all the other precursors. The main difference from the other fuels is the number of the peaks assigned for $^5D_0 \rightarrow {}^7F_4$ transition as it only gives one peak at that of strongest, 705 nm.

Similar to literature studies, 5% of doping gives the most intensive transitions and appears to be the critical doping level [26-28].

3.4.2 Fluorescence Studies for Dy Doped $LaBO_3$

Emission spectra of Dy^{3+} doped $LaBO_3$ were determined at 351 nm excitation. Figure 20 shows the luminescence spectra of Dy^{3+} doped $LaBO_3$. At 351 nm

An analogous study for Tb emission was done by Zhang *et al.* [27]. They found that after 5 % of Tb doping, there is a quenching effect on the emission spectra which is consistent with our work as we observed a critical point after 5% of doping.

Similar to reported studies [22-25], our samples give the most intensive emission peaks at 5% of Tb doping. As a comparison, the intensity of all the transitions follows the order: 5 > 7.5 > 2.5 mol%.

CHAPTER 4

CONCLUSION AND RESULTS

X-Ray patterns of the compounds show that all the $LaBO_3$ products which were synthesized by three different methods are successfully achieved. All the observed patterns of $LaBO_3$ produced with three different methods with all types and amount of doping materials belong to same card number (JCPDS no: 12-0762). In the X-Ray patterns of the products, there are some unidentified peaks around 24, 27.7 and 32 θ degree seen on $LaBO_3$. These peaks were studied in detail and found out that they do not belong to any compounds which have Lanthanum, Europium, Dysprosium or Terbium inside.

REE doped $LaBO_3$ powders show four absorption bands, v1 symmetric stretching, v2 out of plane bending, v3 asymmetric stretching v4 in-plane bending. We observed that some of the products give two peaks for the v2 band at 708, 790 cm^{-1}, and some of them give only one peak for the v2 band at 708 cm^{-1}.

When the size of the product is considered, citric acid gives the smallest size among the other precursors. Particles synthesized by citric acid precursor have around 50 120 nm size while the particles synthesized by glycine have around 100, 200 nm size. $LaBO_3$ powders synthesized by urea precursor have around 500 to 1200 nm size. It is noticed that all the particles tend to agglomerate.

Variations in $LaBO_3$:REE emissions have been observed for the products synthesized by different chelating agents. For Eu, Dy and Tb doping in $LaBO_3$, urea precursor tends to give the best luminescence characteristics. When the best emissions are considered, Eu gives $^5D_0 \rightarrow {}^7F_1$, $^5D_0 \rightarrow {}^7F_2$, $^5D_0 \rightarrow {}^7F_3$ and $^5D_0 \rightarrow {}^7F_3$ transitions, Dy gives $^4F_{9/2} \rightarrow {}^6F_{15/2}$, $^4F_{9/2} \rightarrow {}^6F_{13/2}$ and $^4F_{9/2} \rightarrow {}^6F_{11/2}$ transitions and finally Tb gives $^5D_4 \rightarrow {}^7F_6$, $^5D_4 \rightarrow {}^7F_5$, $^5D_4 \rightarrow {}^7F_3$ and $^5D_4 \rightarrow {}^7F_2$ transitions.

It is found that the luminescence intensity increases as a function of doping agent only for $LaBO_3$:Dy whereas, 5% mole of REE doping is the critical amount for the $LaBO_3$ emission for Tb and Eu.

With the strong XRD patterns and large particle sizes observed by SEM, urea products have very good and large crystalline characteristics which eventually lead them to have better emission intensities.

REFERENCES

1) R. B. Kistler, C., C. Helvaci, *Industrial Minerals and Rocks*, 6th edition, D.D. Carr, Senior Editor, Published by Society for Mining and Metallurgy and Exploration Inc., Littleton, Colerado, 171-186, 1994.

2) Roskill, 2006 – *The Economics of Boron*. 11th Edition, Roskill Information Services Ltd., London, England, Isbn 0 86214 516-3.

3) Eti Maden *2010 Annual Report.*

4) Roskill, *The Economics of Boron*, 10th edition, 2002.

5) D. Trimmnell, B. S. Shasha, R. E. Wing, F. H. Otey. (1982). *J Appl Polym Sc*, 27, 10, 3919–3928.

6) M. B. Buluttekin, *2nd National Economy Conference*, 20-22 February 2008, Izmir.

7) E. Newton, *A history of luminescence from the earliest times until 1900,* 1st edition, Published by American Philosophical Society, Philadelphia,11-13, 1957.

8) A. Jablonski. *Nature* 131, (1933) 839-840.

9) Gilbert, A and Baggott, *J, Essentials of Molecular Photochemistry*, Blackwell Science Ltd, 1990.

10) C.E. Housecroft, A.G. Sharpe, *Inorganic Chemistry*, 1st Ed, PrenticeHall, 2001.

11) Castor, S.B., Hedrick, J.B., 2006; *Rare Earth Elements*. In: Industrial Minerals and Rocks, Littleton.

12) G. Haxel, J. Orris, 2006. *Rare Earth elements crtical resources for high technology*. Restan (VA), United States Geological Survay, USGS 087-02.

13) T. Aitasalo, P. Deren, J. Holsa, H. Jungner, J.-C. Krupa, M. Lastusaari, J. Legendziewicz, J. Niittykoski, W. Strek, *Journal of Solid State Chemistry* 171 (2003) 114–122.

14) M. Gafta , G. Panczer, R. Reisfeld, I. Shinno, *Journal of Alloys and Compounds* (2000) 267 –274.

15) M. A. Zaitoun, *Spectroscopy* 16 (2002) 29–35.

16) K. Annapurna, R.N. Dwivedi, S. Buddhudu, *Materials Letters* 53 (2002) 359– 363.

17) L. Yang, L. Zhou, X. Chen, X. Liu, P.ei Hua, Y. Shi, X. Yue , Z. Tang, Y.Huang, *Solid State ionics*, 509 (2011) 3866-3871.

18) M. Gaft, G. Panczer, R. Reisfeld, I. Shinno, *Journal of Alloys and compounds* (2000) 267–274.

19) N. Koslova, B. Viana and C. Sanchez, *J. Mater. Chem*. 3 (1993), 111.

42) K.A. Singh, L. C. Pathak, S: K. Roy. *Ceramics International* 33 (2007) 1463–1468.

43) D.Y. Chung, E.H. Lee, *J. Alloys Compd.* 374 (2004) 69–73

44) S.D. Han, S:P. Khatkar, V. B Taxak, G. Sharma, D. Kumar., *Mater. Sci. Eng. B* 129 (2006) 126–130.

45) S.Shi, J. H. Hwang, *J. Min. Mat. Char. Eng.,* 2 (2003) 101-110.

46) S.T. Aruna, A.S. Mukasyan*, Curr. Opin. Solid. St. M.* 12 (2008) 44–50.

47) H. J. FEng, J. J. Moore, D. G. Wirth, *Metall. Mater. Trans. A*, 23 (2012) 2373-2379.

48) O. D. Michael, ed. *The Encyclopedia of Minerals and Gemstones.* London: Orbis Publishing, 1985.

49) F. Liu, S. Zuo, W. Kong, C. Qi., *Green Chem.,* 14 (2012), 1342-1349.

50) S. D. Dunmead, Z. A. Munir, J. B. Holt and D. D. Kingman, *J. Mater. Sci.* 26, (1991) 2410.

51) Alain C. Pierre, *Introduction to Sol-Gel Processing*, Kluwer Academic Publishers, London 1998.

52) M. Tukia, J. Hölsa, M. Lastusaari, J. Niitykoski, *Opt Mater, 27* (2005) 1516-1522.

53) F. Li, K. Hu, D. Zhang, G. Chen, *J. Nucl. Mater,. 300* (2002) 1 82-88.

54) H. Mohebbi, T. Ebadzadeh, F.A. Hesari, *Powder Technol. 188* (2009) 183-186

55) N. R. Noori, R. S. Mamoory, P. Alizadeh, A. Mehdikhani, J. Ceram. Process. Res., 9 (2008) 246-249.

56) Y. Pan, M. Wu, Q. Su, *Mater. Sci. Eng., 106* (2004) 251-256.

57) J. Gomes, A. M. Pires, O. A. Serra, *J Fluoresc 16* (2006) 411–421.

58) L. Xu, B. Wei, Z. Zhang, Z. Lu, H. Go, Y. Zhang, *Nanotechnology 17* (2006) 4327-4331.

59) C. F. Bacalski, M. A. Cherry, G. A. Hiruta, J. M. McKittrick, J. Mourant, *J. SID Supp.-1,* (2000) 93-98.

60) Y. T. Wu, L. S. Qin, H. S. Shi, Y. Zhang, Y. X. Yang, K. Y. Shu, IEEE T. Nucl. Sci. 57 (2010) 1343-1347.

APPENDIX

APPENDIX A

X-RAY Diffraction Data

Table 9: X-Ray Diffraction data of pure $LaBO_3$ by citric acid, JCPDS no: 12-0762.

Observed Data			Card Peak			
2theta degree	d-value	Intensity (cps)	2theta	d-value	Intesity (I/Io)	Hkl
20.5	4.32865	280	20.45	4.339	20	011
21.6	4.11063	98	21.5	4.13	10	020
23.0	3.56349	32				
25.5	3.4901	1904	25.49	3.492	100	111
26.4	3.37312	844	26.37	3.377	55	120
29.5	3.02533	37				
30.4	2.93778	398	30.42	2.936	20	200
31.8	2.81157	34	31.68	2.822	2	121
32.4	2.76086	88	32.33	2.767	8	210
34.1	2.63	151				
35.2	2.54739	250	35.12	2.553	20	002
37.1	2.42118	565	37.06	2.424	25	031
37.6	2.39012	174	37.54	2.394	14	220
40	2.25207	23	40.01	2.252	10	112
41.6	2.16908	173	41.52	2.173	12	022
44.5	2.03422	707	44.44	2.037	45	122
46.7	1.94339	210	46.61	1.947	20	140
47.2	1.92396	222	47.12	1.927	20	202
48.7	1.86815	479	48.68	1.869	30	231
51.2	1.78264	383	51.13	1.785	20	311

Table 9: X-Ray Diffraction data of pure $LaBO_3$ by citric acid, JCPDS no: 12-0762 (cont'd).

Observed Data			Card Peak			
2theta degree	d-value	Intensity (cps)	2theta	d-value	Intesity (I/Io)	hkl
52.4	1.74461	68	52.36	1.746	8	222
			54.23	1.69	6	240
			55.02	1.6676	6	013
57.5	1.6014	126	57.4	1.6039	14	113
59.7	1.54753	115	59.67	1.5482	12	142
61.1	1.51538	114	61	1.5176	10	151
63.3	1.46791	31	63.3	1.4679	6	400
64.1	1.4151	85	63.98	1.4539	6	322
			64.19	1.4497	12	213
65.8	1.41806	19	65.66	1.4207	4	340
66.4	1.4067	42	66.31	1.4084	6	242
67.3	1.39006	47	62.27	1.3906	8	411
			67.68	1.3832	4	420
			68.06	1.3764	4	060
72.8	1.298	103	72.77	1.2985	10	233
			74.2	1.2769	6	004

Table 10: X-Ray Diffraction data of pure $LaBO_3$ by glycine, JCPDS no: 12-0762.

Observed Data			Card Peak			
2theta degree	d-value	Intensity (cps)	2theta	d-value	Intensity (I/Io)	hkl
20.6	4.30786	274	20.451	4.339	20	011
			21.497	4.13	10	020
23.0	3.56349	32				
25.6	3.47669	1474	25.486	3.492	100	111
26.5	3.36062	725	26.369	3.377	55	120
29.5	3.02533	37				
30.5	2.92838	261	30.419	2.936	20	200
			31.679	2.822	2	121
32.4	2.76086	59	32.326	2.767	8	210
34.1	2.63	151				
35.3	2.54041	201	35.12	2.553	20	002
35.3	2.54041	201	35.206	2.547	12	201
36.1	2.48592	24	35.994	2.493	2	130
			36.913	2.433	40	211
37.2	2.4149	453	37.055	2.424	25	031
37.7	2.38401	141	37.537	2.394	14	220
			40.001	2.252	10	112
41.7	2.16411	133	41.521	2.173	12	022
43.8	2.06509	30	43.78	2.066	8	040
44.6	2.02989	528	44.436	2.037	45	122
46.7	1.64339	188	46.608	1.947	20	140
47.3	1.92012	176	47.121	1.927	20	202
48.8	1.86455	406	48.676	1.869	30	231
51.3	1.7794	275	51.128	1.785	50	311
51.8	1.7634	126	51.655	1.768	14	320
52.5	1.74152	54	52.355	1.746	8	222
54.4	1.6851	33	54.229	1.69	6	240
55.2	1.66255	23	55.019	1.6676	6	013
57.6	1.59886	136	57.402	1.6039	14	113
59.8	1.54518	115	59.672	1.5482	12	142
61.1	1.54538	100	61.001	1.5176	10	151
63.3	1.46791	18	63.3	1.4679	6	400
64.1	1.4512	71	63.982	1.4539	6	322

Table 10: X-Ray Diffraction data of pure $LaBO_3$ by glycine, JCPDS no: 12-0762 (cont'd).

Observed Data			Card Peak			
2theta degree	d-value	Intensity (cps)	2theta	d-value	Intesity (I/Io)	hkl
65.7	1.41998	21	65.662	1.4207	4	340
66.4	1.4067	37	66.309	1.4084	6	242
67.4	1.38824	47	67.27	1.3906	8	411
67.7	1.38281	41	67.678	1.3832	4	420
68.2	1.37389	23	68.058	1.3764	4	060
72.9	1.29646	97	82.767	1.2985	10	233
74.4	1.27399	51	74.202	1.2769	6	004

Table 11: X-Ray Diffraction data of pure $LaBO_3$ by urea, JCPDS no: 12-0762.

Observed Data			Card Peak			
2theta degree	d-value	Intensity (cps)	2theta	d-value	Intensity (I/Io)	hkl
			20.451	4.339	20	011
			21.497	4.13	10	020
23.0	3.56349	32				
			25.486	3.492	100	111
			26.369	3.377	55	120
29.5	3.02533	37				
30.6	2.91904	317	30.419	2.936	20	200
34.1	2.63	151				
			35.12	2.553	20	002
35.4	2.53346	337	35.206	2.547	12	201
36	2.4926	22	35.994	2.493	2	130
			36.913	2.433	40	211
			37.055	2.424	25	031
			37.537	2.394	14	220
40.2	2.24133	34	40.001	2.252	10	112
41.7	2.16411	115	41.521	2.173	12	022
44	2.05617	70	43.78	2.066	8	040
			44.436	2.037	45	122
46.8	1.93947	303	46.608	1.947	20	140
47.3	1.92012	290	47.121	1.927	20	202
			48.511	1.875	4	212
48.9	1.86097	551	48.676	1.869	30	231
51.3	1.7794	357	51.128	1.785	20	311
51.8	1.7634	176	51.655	1.768	14	320
			52.355	1.746	8	222
55.2	1.66255	51	55.019	1.6676	6	013
57.6	1.59886	213	57.402	1.6039	14	113
59.9	1.54284	167	59.672	1.5482	12	142
61.2	1.51315	151	61.001	1.5176	10	151
63.4	1.46584	30	63.3	1.4679	6	400
64.2	1.44949	103	64.189	1.4539	12	213
65.8	1.41806	31	65.662	1.4207	4	340
66.5	1.40482	50	66.309	1.4084	6	242

Table 11: X-Ray Diffraction data of pure $LaBO_3$ by urea, JCPDS no: 12-0762 (cont'd).

Observed Data			Card Peak			
2theta degree	d-value	Intensity (cps)	2theta	d-value	Intensity (I/Io)	hkl
67.8	1.38102	63	67.678	1.3832	4	420
68.3	1.37212	32	68.058	1.3764	4	060
73	1.29493	143	72.767	1.2985	10	233
			74.202	1.2769	6	004

Table 12: X-Ray Diffraction data of 7.5% Tb doped $LaBO_3$ by urea, JCPDS no: 12-0762.

Observed Data			Card Peak			
2theta degree	d-value	Intensity (cps)	2theta	d-value	Intensity (I/Io)	hkl
20.6	4.30786	314	20.451	4.339	20	011
			21.497	4.13	10	020
23.0	3.56349	32				
25.6	3.47669	2205	25.486	3.492	100	111
26.5	3.36062	1110	26.369	3.377	55	120
29.5	3.02533	37				
30.5	2.9238	313	30.419	2.936	20	200
			31.679	2.822	2	121
32.4	2.76086	73	32.326	2.767	8	210
34.1	2.63	151				
			35.12	2.553	20	002
35.3	2.54041	318	35.206	2.547	12	201
36.1	2.48592	40	35.994	2.493	2	130
37	2.42749	429	36.913	2.433	40	211
37.2	2.4149	536	37.055	2.424	25	031
37.6	2.39011	213	37.537	2.394	14	220
40.1	2.24669	34	40.001	2.252	10	112
			41.521	2.173	12	022
			43.78	2.0366	8	040
44.6	2.02989	644	44.436	2.037	45	122
46.7	1.94339	243	46.608	1.947	20	140
47.2	1.92396	296	47.121	1.927	20	202
			48.511	1.875	4	212
48.8	1.86455	457	48.676	1.869	30	231
51.1	1.7859	311	51.128	1.785	20	311
51.7	1.76657	168	51.655	1.768	14	320
52.5	1.74152	67	52.355	1.746	8	222
54.3	1.68797	38	54.229	1.69	6	240
57.5	1.6014	177	57.402	1.6039	14	113
59.8	1.54518	148	59.672	1.5482	12	142
			61.001	1.5176	10	151
			63.3	1.4679	6	400

Table 12: X-Ray Diffraction data of 7.5% Tb doped $LaBO_3$ by urea, JCPDS no: 12-0762 (cont'd).

Observed Data			Card Peak			
2theta degree	d-value	Intensity (cps)	2theta	d-value	Intensity (I/Io)	hkl
			64.189	1.4494	12	213
65.8	1.41806	27	65.662	1.4207	4	340
66.4	1.4067	44	66.309	1.4084	6	242
			67.27	1.3906	8	411
67.7	1.38281	55	67.678	1.38832	4	420
68.2	1.3789	27	68.058	1.3764	4	060
72.9	1.29464	107	72.767	1.2985	10	233
74.4	1.27399	74	74.202	1.2769	6	004